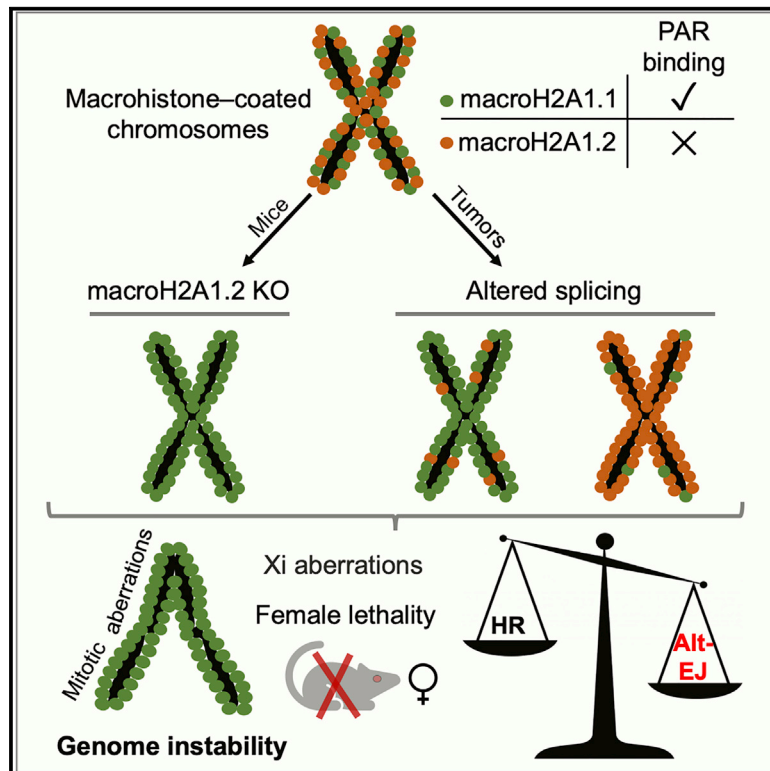


Epigenetic Regulation of DNA Repair Pathway Choice by MacroH2A1 Splice Variants Ensures Genome Stability

Graphical Abstract



Authors

Robin Sebastian, Eri K. Hosogane, Eric G. Sun, ..., Yves Pommier, Mirit I. Aladjem, Philipp Oberdoerffer

Correspondence

robin.sebastian@nih.gov (R.S.), philipp.oberdoerffer@nih.gov (P.O.)

In Brief

Sebastian et al. demonstrate that balanced expression of macroH2A1 splice variants is essential to ensure genome integrity. Deletion of macroH2A1.2 in mice results in X chromosome instability through aberrant alternative end joining mediated by macroH2A1.1. MacroH2A1 splice variant imbalance is also predictive of DNA repair outcome in cancer cells.

Highlights

- The macroH2A1.2 histone variant promotes Xi stability and female survival in mice
- Balanced macroH2A1 splice variant expression ensures genome integrity
- MacroH2A1.1 promotes alt-EJ and genome instability in macroH2A1.2 knockout mice
- MacroH2A1 splice variants affect DNA repair pathway choice in cancer cells

Article

Epigenetic Regulation of DNA Repair Pathway Choice by MacroH2A1 Splice Variants Ensures Genome Stability

Robin Sebastian,^{1,3,*} Eri K. Hosogane,^{1,4} Eric G. Sun,^{1,5} Andy D. Tran,¹ William C. Reinhold,³ Sandra Burkett,² David M. Sturgill,¹ Prabhakar R. Gudla,¹ Yves Pommier,³ Mirit I. Aladjem,³ and Philipp Oberdoerffer^{1,6,7,*}

¹Laboratory of Receptor Biology and Gene Expression, National Cancer Institute, NIH, Bethesda, MD 20892, USA

²Molecular Cytogenetics Core Facility, National Cancer Institute, Frederick, MD 21702, USA

³Developmental Therapeutics Branch, National Cancer Institute, NIH, Bethesda, MD 20892, USA

⁴Present address: Department of Informative Genetics, Environment and Genome Research Center, Tohoku University Graduate School of Medicine, Sendai 980-8575, Japan

⁵Present address: Department of Genetics and Yale Stem Cell Center, Yale School of Medicine, New Haven, CT 06520, USA

⁶Present address: Division of Cancer Biology, National Cancer Institute, NIH, Rockville, MD 20850, USA

⁷Lead Contact

*Correspondence: robin.sebastian@nih.gov (R.S.), philipp.oberdoerffer@nih.gov (P.O.)

<https://doi.org/10.1016/j.molcel.2020.06.028>

SUMMARY

The inactive X chromosome (Xi) is inherently susceptible to genomic aberrations. Replication stress (RS) has been proposed as an underlying cause, but the mechanisms that protect from Xi instability remain unknown. Here, we show that macroH2A1.2, an RS-protective histone variant enriched on the Xi, is required for Xi integrity and female survival. Mechanistically, macroH2A1.2 counteracts its structurally distinct and equally Xi-enriched alternative splice variant, macroH2A1.1. Comparative proteomics identified a role for macroH2A1.1 in alternative end joining (alt-EJ), which accounts for Xi anaphase defects in the absence of macroH2A1.2. Genomic instability was rescued by simultaneous depletion of macroH2A1.1 or alt-EJ factors, and mice deficient for both macroH2A1 variants harbor no overt female defects. Notably, macroH2A1 splice variant imbalance affected alt-EJ capacity also in tumor cells. Together, these findings identify macroH2A1 splicing as a modulator of genome maintenance that ensures Xi integrity and may, more broadly, predict DNA repair outcome in malignant cells.

INTRODUCTION

Susceptibility to genome instability is intimately linked to the surrounding chromatin environment (Dabin et al., 2016). A prominent example is the highly condensed, inactive X chromosome (Xi), which acts as an epigenetic hotspot for genomic aberrations. Compared to autosomes and its active counterpart (Xa), the Xi exhibits elevated risk for genome instability in the form of chromosome loss, micronuclei formation, and mutation during aging and malignancy (Jäger et al., 2013; Machiela et al., 2016; Russell et al., 2007). The Xi is characterized by a repressive chromatin environment, which ensures dosage compensation of X-linked gene expression in female mammals but interferes with DNA replication initiation. As a result, the Xi is among the latest replicating chromosomes and its unique replication dynamics have been associated with increased susceptibility to replication stress (RS) (Koren and McCarroll, 2014). Accumulation of under-replicated DNA can cause DNA fragility and DNA double-strand breaks (DSBs) in late S/G2, pointing to RS as a likely

contributor to Xi-specific genome instability (Bakhoun et al., 2017; Minocherhomji et al., 2015). The mechanisms that protect female cells from this inherent Xi instability remain to be investigated.

RS is epigenetically modulated by the homologous recombination (HR)-promoting macroH2A1.2 histone variant, which forms protective chromatin domains across fragile DNA (Khurana et al., 2014; Kim et al., 2018). Both macroH2A1.2 and its alternative splice variant, macroH2A1.1, are enriched on the mammalian Xi to form the Xi macro-body (Costanzi and Pehrson, 1998) (Figure S1A). Of note, macro-histones are dispensable for initiation and maintenance of X chromosome inactivation (XCI) (Changolkar et al., 2007), and the functional relevance of Xi-enriched macro-histones remains elusive. Here, we investigate macroH2A1.2 function using a splice-variant-specific knockout (KO) mouse model. We identify a novel, splicing-modulated role for macroH2A1 variants in genome maintenance, which provides a rationale for macroH2A1.2 accumulation on the Xi and has implications not only for Xi integrity

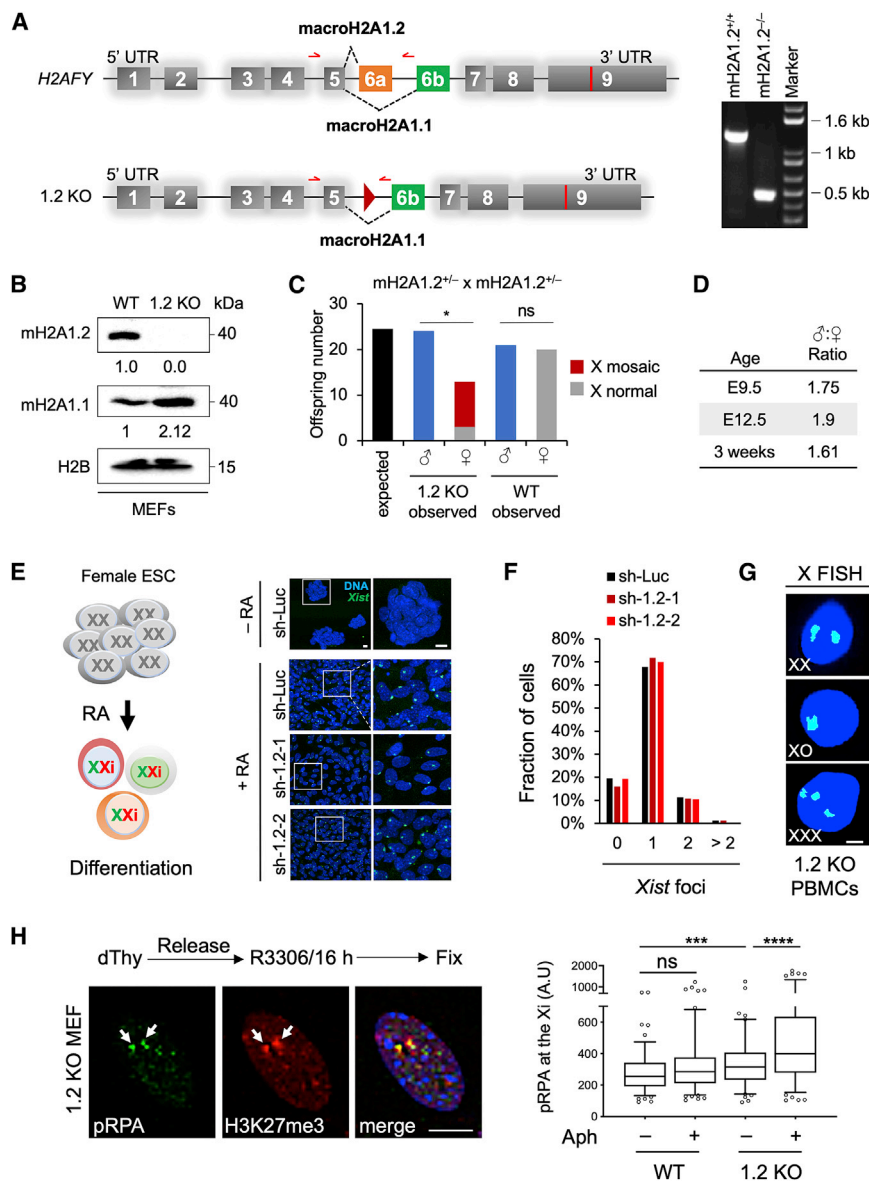


Figure 1. MacroH2A1.2 Loss Impairs Female Survival and X Ploidy

(A) Schematic of the macroH2A1-encoding H2AFY gene and the macroH2A1.2 KO allele (1.2 KO) (not to scale). Exon 6a was deleted by Cre/loxP-mediated recombination, resulting in a residual loxP site (triangle). Alternative splicing resulting in macroH2A1.1 or macroH2A1.2 is indicated. Red arrows depict primers used for PCR genotyping, resulting in a 1.3-kb fragment for the WT allele and a 0.5-kb fragment for the 1.2 KO allele. A representative PCR for the indicated genotypes is shown.

(B) Western blot for macroH2A1 variants in MEFs from WT and 1.2 KO littermates.

(C) Number of WT and 1.2 KO males and females at time of weaning, based on 28 litters from macroH2A1.2^{-/-} parents. X mosaicism was determined as in (G) for all female KO offspring and a subset of male KO and female WT offspring (see Figure S1O). *p = 0.01, based on a two-tailed binomial test; ns, not significant.

(D) Male-to-female ratio in 1.2 KO mice analyzed at the indicated ages. Two-way comparisons between each of the three age groups revealed no significant differences based on Fisher's exact test.

(E) Xist induction in differentiating female mouse ESCs expressing a control short hairpin RNA (shRNA) (sh-Luc, n = 218 cells) or one of two distinct shRNAs against macroH2A1.2, sh-1.2-1 (n = 260 cells) and sh-1.2-2 (n = 379 cells) (see Table S2 for shRNA sequences). A schematic for retinoic-acid-induced ESC differentiation is shown. Xist was detected by RNA FISH, nuclei were stained with Hoechst 33342, and representative images and enlarged inlays are shown. Scale bars, 10 μm.

(F) Fraction of cells with the indicated number of Xist foci, based on (E).

(G) X chromosome FISH in PBMCs from 1.2 KO mice. Female cells with X counts other than XX were considered X mosaic. Scale bar, 10 μm.

(H) Representative colF images and quantification showing pRPA localization to the Xi. H3K27me3 is used to mark the Xi (white arrows). A minimum of 100 cells were analyzed per group. Scale bar, 10 μm. ***p < 0.001 and ****p < 0.0001, based on Mann-Whitney U test.

See also Figure S1 and Table S2.

but also more broadly for DNA repair pathway control in malignant cells.

RESULTS

MacroH2A1.2 Ensures Anaphase Integrity and Female Viability

To selectively inactivate macroH2A1.2, we generated splice-variant-specific KO mice via targeted inactivation of the macroH2A1.2-encoding exon 6a in embryonic stem cells (ESCs). MacroH2A1.2 expression was undetectable in macroH2A1.2^{-/-} mice, while expression of the macroH2A1.1 variant was increased by ~2-fold both at the overall RNA/protein level and

on the Xi, consistent with exclusive and compensatory use of the macroH2A1.1-encoding exon 6b (Figures 1A, 1B, and S1B–S1D). MacroH2A1.2-deficient male mice were born at the expected rate. However, female macroH2A1.2^{-/-} mice were 40–50 % less frequent than males (Figures 1C, 1D, and S1E). Loss of females was observed as early as embryonic day 9.5 (E9.5) with a male-to-female ratio of 1.75 at E9.5 and 1.9 at E12.5 (Figure 1D), indicative of a female-biased, developmental defect. Similar to previous findings in mice lacking both macroH2A1 splice variants (Changolkar et al., 2007), ablation of macroH2A1.2 did not interfere with XCI, as (1) expression and spreading of the XCI-initiating Xist non-coding RNA occurred normally in the absence of macroH2A1.2 in two distinct

ESC-based XCI models (Figures 1E, 1F, and S1F–S1N) (Engreitz et al., 2013; Jonkers et al., 2008), and (2) repression of Xi-linked genes in differentiating, macroH2A1.2-deficient ESCs was comparable to wild-type (WT) cells (Figure S1F). Female-biased embryonic lethality in the absence of XCI defects has been observed previously as a result of aberrant replication and concomitant genome instability (McNairn et al., 2019). Supporting a role for macroH2A1.2 in the latter, the majority of surviving macroH2A1.2^{-/-} females showed varying levels of X aneuploidy in peripheral blood mononuclear cells (PBMCs) (Figures 1C, 1G, and S1E). No X aneuploidy was detected in PBMCs from KO males or WT females (Figure S1O). Since numerical chromosomal aberrations have been linked to RS in both yeast and humans (Ait Saada et al., 2017; Burrell et al., 2013), we asked if macroH2A1.2 loss promotes RS at the Xi. Using co-immunofluorescence (coIF) analysis for phosphorylated single-stranded DNA-binding protein RPA32 (pRPA), a marker of RS (Maréchal and Zou, 2015), and trimethylated histone H3K27, a marker for the Xi (Plath et al., 2003), we observed a significant increase in Xi-associated RS in macroH2A1.2-deficient, but not WT mouse embryonic fibroblasts (MEFs) arrested at G2/M following treatment with a low dose of the DNA polymerase inhibitor aphidicolin (Figure 1H). Together, these findings uncover a role for macroH2A1.2 in protecting from Xi-associated RS, Xi aneuploidy, and female-biased lethality.

MacroH2A1.2 Loss Promotes Xi-Associated Anaphase Instability

Aneuploidy is the result of defective anaphase progression. To determine if macroH2A1.2 helps ensure anaphase integrity, we first measured the overall frequency of mitotic aberrations including DNA bridges and lagging chromosomes in MEFs from both WT and macroH2A1.2^{-/-} mice. MacroH2A1.2 deficiency caused a pronounced increase in anaphase defects (Figures 2A and 2B), which were further aggravated by treatment with etoposide, an inhibitor of type II topoisomerases (TOP2) that interferes with decatenation of under-replicated genomic DNA to promote DNA fragility (Downes et al., 1994) (Figures 2A and 2B). Treatment with etoposide was restricted to 1 h prior to cell harvest, pointing to DSB formation in G2/M as the main cause for etoposide-induced anaphase defects. Anaphase defects further coincided with increased accumulation of cells in G2 and a reduction in mitotic index, supporting a defect in mitotic entry or progression (Figures S2A and S2B). The majority of anaphase bridges and lagging chromosomes did not contain centromeres, ruling out kinetochore-related segregation defects (Figure S2C). Together, these observations identify a role for macroH2A1.2 in the suppression of anaphase bridge formation.

To determine whether macroH2A1.2-loss-associated anaphase defects are biased toward the Xi, we performed selective spectral karyotyping using fluorescence *in situ* hybridization (FISH) probe sets specific for either the X chromosome or a comparably sized autosome, chromosome 2. Chromosome X accounted for ~60% of all DNA bridges or lagging chromosomes in anaphases from etoposide-treated macroH2A1.2^{-/-} MEFs compared to ~30% in WT cells (Figure 2C). In contrast, anaphase defects involving chromosome 2 were comparable between WT and macroH2A1.2^{-/-} MEFs and represented ~5% of all DNA bridges, as

expected based on chromosome size. Moreover, the frequency of X-specific anaphase aberrations in male MEFs was unaffected by macroH2A1.2 deletion and was overall significantly lower than in females, consistent with the Xi being less stable than the Xa (Figure 2C) (Jäger et al., 2013; Machiela et al., 2016; Russell et al., 2007). Increased Xi-anaphase defects were further observed upon ionizing radiation (IR) and persisted into the subsequent G1 phase in the form of macro-body-associated, nucleoplasmic bridges (Figures 2D and S2D).

Aberrant formation and/or resolution of anaphase bridges can cause chromosome mis-segregation, aneuploidy, and micronuclei accumulation (Bakhoum et al., 2017). Spectral karyotyping of macroH2A1.2-deficient metaphase MEFs revealed an increase in aneuploidy that was most pronounced for X chromosomes (Figures 2E and 2F), consistent with our findings in PBMCs from surviving macroH2A1.2^{-/-} female mice. Little to no aneuploidy was observed in WT cells. Moreover, macroH2A1.2 loss resulted in a 5-fold increase in micronuclei formation in response to etoposide-induced DSB formation in G2/M compared to WT cells (Figures 2G and 2H). FISH analysis of the same cells revealed both increased X-chromosome-positive micronuclei and X aneuploidy (Figures 2G and 2I). Micronuclei from macroH2A1.2^{-/-} MEFs were also significantly enriched for the Xi chromatin mark H3 trimethyl-K27 (Figure S2E) (Jäger et al., 2013). Together, these observations support the notion that anaphase aberrations involving the late-replicating Xi promote enhanced genome instability, which may be at least in part responsible for female-biased lethality of macroH2A1.2-deficient mice.

Variant-Specific Proteomes Reveal a Role for MacroH2A1.1 in Alternative End Joining (Alt-EJ)

The above findings stand in sharp contrast to previous reports in mice deficient in both macroH2A1 splice variants, which show no overt defects in female survival or genome integrity (Changolkar et al., 2007). We thus considered the possibility that the phenotypes observed in macroH2A1.2^{-/-} MEFs and mice may be a consequence of unbalanced macroH2A1.1 function. Consistent with this notion, macroH2A1 splice variants have opposing roles in various cellular processes, including the control of HR and cell growth (Chen et al., 2015; Khurana et al., 2014; Kim et al., 2019). MacroH2A1 splice variants differ in 33 aa within the macrodomain, which allows macroH2A1.1, but not macroH2A1.2, to bind ADP-ribose derivatives (Kustatscher et al., 2005).

To understand the molecular basis for differential macroH2A1 splice variant functions, we sought to comprehensively interrogate variant-specific protein interactomes. FLAG-tagged macroH2A1 cDNA (F-mH2A1) was targeted into a single genomic locus in HEK293 T-REx cells, ensuring expression levels comparable to WT macroH2A1.2. Note that endogenous macroH2A1.1 is poorly expressed in immortalized cells, including HEK293 cells (Figures 3A and S3A). Nuclear protein lysates from F-mH2A1.1- and F-mH2A1.2-expressing cell lines were subjected to FLAG coimmunoprecipitation (coIP), followed by differential dimethyl labeling using CH₂O (light) and CD₂O (medium), respectively (Figure 3A). CoIP specificity was validated using H2B as positive control and Proliferating Cell Nuclear Antigen (PCNA) as negative control (Figure 3B). Subsequent comparative mass spectrometry (MS) analysis of two

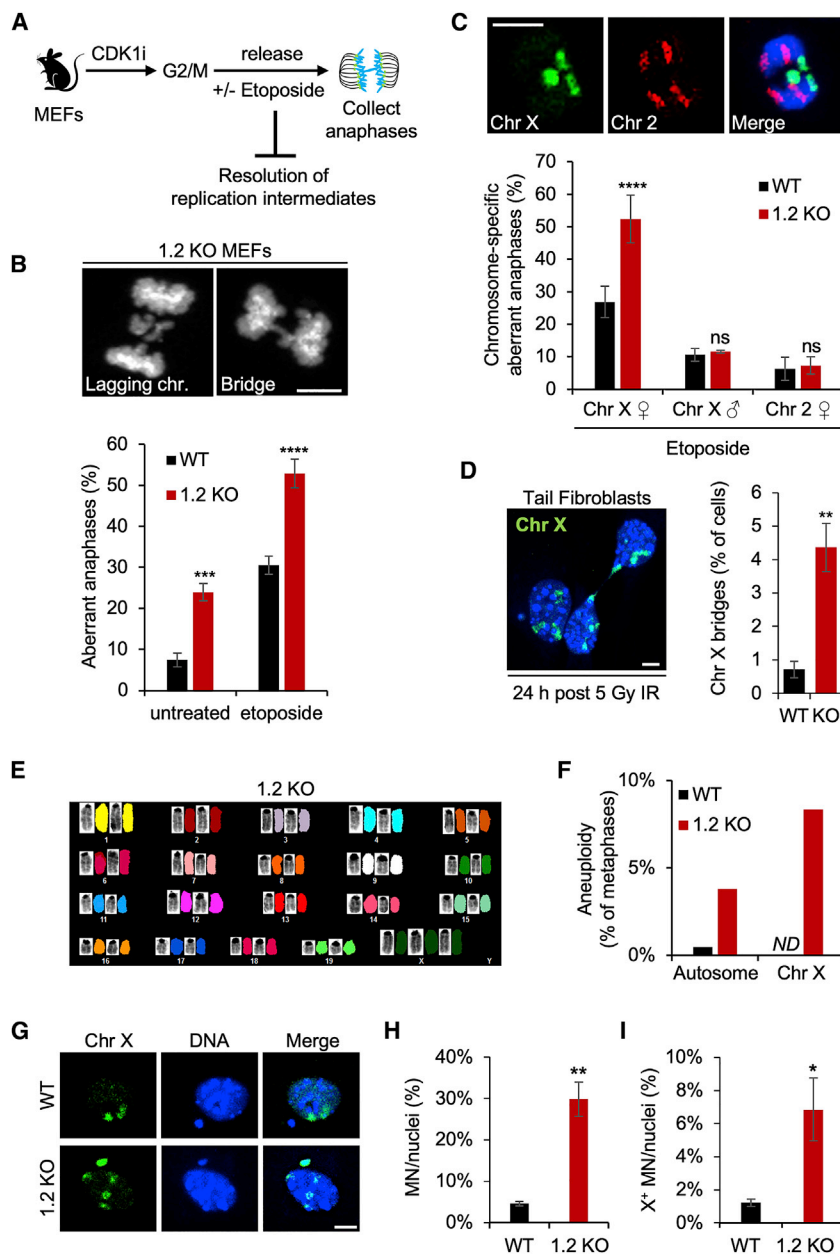


Figure 2. MacroH2A1.2 Protects from Xi-Specific Anaphase Defects and Chromosomal Instability

(A) Schematic for anaphase collection. MEFs from WT or macroH2A1.2 KO (1.2 KO) mice were arrested at G2/M via inhibition of CDK1 (CDK1i), followed by release in the presence or absence of etoposide and analysis 50 min thereafter.

(B) Frequency of anaphase aberrations in WT or 1.2 KO MEFs in the presence or absence of etoposide. At least 70 metaphases were analyzed per sample, and representative images for lagging chromosomes and DNA bridges are shown. Scale bar, 10 μ m.

(C) Frequency of X- or chromosome-2-specific anaphase aberrations expressed as percentage of total aberrant anaphases in male or females MEFs treated with etoposide. Representative FISH images are shown. Scale bar, 10 μ m. At least 50 metaphases were analyzed per sample.

(D) Frequency of X chromosome bridges in asynchronous WT and 1.2 KO mouse tail fibroblasts 24 h after 5 Gy of IR. At least 100 metaphases were analyzed per sample, and a representative FISH image is shown. DNA was counterstained with Hoechst 33342. Scale bar, 10 μ m.

(E) Representative spectral karyotype (SKY) analysis of a 1.2 KO metaphase with X aneuploidy. Chromosome-specific FISH paints unambiguously identify all 22 mouse chromosomes.

(F) Frequency of autosomal or X chromosomal aneuploidy in WT (n = 34 metaphases) and 1.2 KO MEFs (n = 36 metaphases) based on SKY analysis in (E). One of two representative experiments is shown. ND, not detected. Autosomes with one or more aneuploidy events across 34 metaphases include chromosomes 1, 3, 5, 6, 8, 9, 10, 12, 13, 14, 16, 17, and 19.

(G) X-FISH counterstained with DAPI identifies X⁺ micronucleus and X aneuploidy in 1.2 KO MEF nuclei. A WT nucleus with an X⁻ micronucleus is shown as a control. Scale bar, 10 μ m.

(H and I) Fraction of total (H) and X⁺ MN/nuclei (I) in WT and 1.2 KO MEFs following etoposide treatment, normalized to total cell number and mitotic index (see Figure S2B).

Values are expressed as mean and SD from three independent fibroblast preparations. *p < 0.05, **p < 0.01, ***p < 0.001, and ****p < 0.0001, based on Student's two-tailed t test. See also Figure S2.

independent colP experiments identified 314 common interactors, including known macroH2A1-binding proteins such as core histones and the Facilitates Chromatin Transcription (FACT) chaperone complex (Table S1; Figure 3C) (Kim et al., 2018). Only four macroH2A1 interactors exhibited a reproducible, greater than 2-fold preference for macroH2A1.1: poly(ADP-ribose) polymerase 1 (PARP1), arginine- and serine-rich coiled-coil 2 (RSRC2), tyrosyl-DNA phosphodiesterase 1 (TDP1), and DNA ligase 3 (LIG3). With an ~4-fold enrichment over macroH2A1.2, LIG3 showed the strongest macroH2A1.1 preference, which was independently confirmed by western blot (Figure 3D). LIG3 interaction with macroH2A1.1 was sensitive to PARP inhibition (Figures 3D and S3B), and a similar effect

was observed for PARP1, in agreement with earlier reports (Ouararhni et al., 2006; Timinszky et al., 2009) (Figure 3D). Moreover, all four macroH2A1.1 interactors were previously shown to be poly-ADP-ribosylated (Gibson et al., 2016; Jungmichel et al., 2013), suggesting that macroH2A1.1-specific binding involves its poly(ADP-ribose)-binding domain (Kustatscher et al., 2005).

Two of the four macroH2A1.1 interactors (LIG3 and PARP1) are centrally involved in alt-EJ, a DNA-end-resection-dependent, microhomology-mediated DNA repair pathway that frequently results in chromosomal aberrations and mutations (Gostissa et al., 2011). Consistent with a role for macroH2A1.1 in this repair pathway, small interfering RNA (siRNA)-mediated macroH2A1.1 depletion caused a significant reduction in alt-EJ

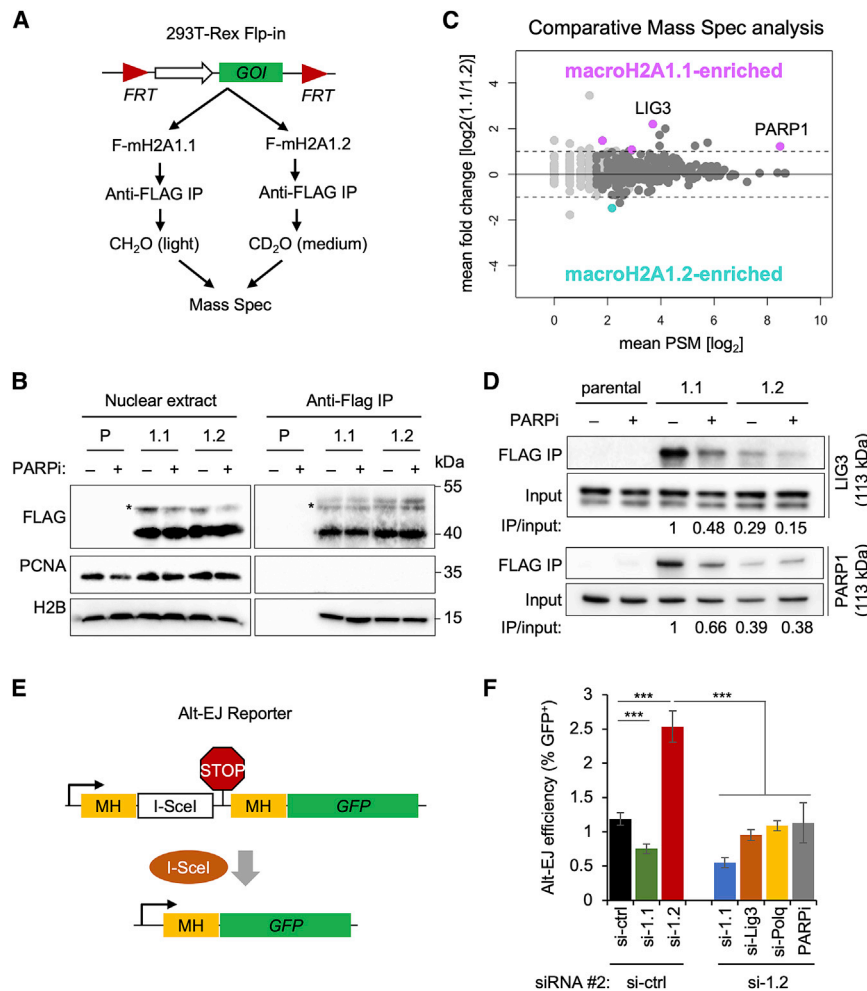


Figure 3. Splice Variant Interactomes Identify MacroH2A1.1 as a Mediator of Alt-EJ

(A) Schematic for macroH2A1 splice variant interactome isolation and comparative MS. HEK293 T-Rex cells carrying a single-copy cDNA encoding of FLAG-macroH2A1.1 (F-mH2A1.1) or FLAG-macroH2A1.2 (F-mH2A1.2) inserted via Flp recombination were subjected to FLAG immunoprecipitation (FLAG-IP), followed by stable isotope dimethyl labeling and combined MS. GOI, gene of interest.

(B) Western blot for the indicated proteins in nuclear lysates or FLAG-IP lysates from parental (P) and macroH2A1 splice-variant-transgenic HEK293 T-Rex cells (1.1, 1.2), in the presence or absence of a PARP inhibitor (PARPi). Asterisks indicate monoubiquitinated F-mH2A1 isoforms (Kim et al., 2017).

(C) Analysis of macroH2A1 splice variant interactomes from (A). Data points reflect mean peptide-spectrum match (PSM) and log₂ fold changes from two independent MS experiments. Proteins with a PSM > 0 are shown, proteins with PSM > 2 are depicted in dark gray, and proteins with a log₂ fold change ≥ 1 and a PSM > 2 in both replicates are shown in pink (macroH2A1.1-enriched) or teal (macroH2A1.2-enriched).

(D) Western blot analysis for LIG3 (top panels) and PARP1 (bottom panels) following FLAG-IP as in (B) in the presence or absence of PARPi. Signal intensities were normalized to input and are expressed relative to the untreated macroH2A1.1 IP sample. One of two independent experiments is shown.

(E) Schematic for alt-EJ reporter assay. A stop codon (STOP) flanked by microhomologies (MHs) prevents GFP expression. DSB induction by the endonuclease I-SceI and subsequent repair by alt-EJ deletes the stop codon and activates GFP expression.

(F) Alt-EJ efficiency in reporter cells expressing a control siRNA (si-ctrl) or a siRNA against macroH2A1.2 (si-1.2), combined with PARPi or a second siRNA, against macroH2A1.1 (si-1.1), LIG3 (si-Lig3) or POLQ (si-Polq). Alt-EJ efficiency is expressed as the fraction of GFP⁺ cells. Values represent mean and SD (n = 3 replicates). ***p < 0.001, based on Student's two-tailed t test.

See also Figure S3 and Table S1.

frequency in a fluorescence-activated cell sorting (FACS)-based reporter assay (Bennardo et al., 2008) (Figures 3E, 3F, and S3C). In contrast, depletion of the HR-permissive macroH2A1.2 variant increased alt-EJ efficiency more than 2-fold in a manner that was entirely dependent on the presence of macroH2A1.1 and the alt-EJ effectors LIG3 and POLQ (Ceccaldi et al., 2015; Gostissa et al., 2011; Mateos-Gomez et al., 2015) (Figures 3F and S3C). Depletion of either variant had only a minor and comparable effect on canonical non-homologous end joining (cNHEJ; Figures S3D and S3E) (Bennardo et al., 2008). Together with our previous work (Khurana et al., 2014; Kim et al., 2018, 2019), these findings thus identify macroH2A1 as a splicing-modulated, epigenetic regulator of repair outcome at resected DNA ends.

Alt-EJ and MacroH2A1.1 Account for MacroH2A1.2-Loss-Induced Anaphase Defects

Next, we asked whether macroH2A1.1 function in alt-EJ may be responsible for the anaphase defects observed in the absence of

macroH2A1.2. While neither HR nor classical NHEJ is active in mitosis (Lee et al., 2014; Orthwein et al., 2014), a recent report has identified a role for alt-EJ in the microhomology-mediated joining of DNA ends after replication fork breakage in mitotic extracts (Deng et al., 2019). Aberrant activation of alt-EJ may thereby account for chromosome fusions of mitotic DSBs, resulting in increased anaphase aberrations. To test this hypothesis, we assessed anaphase defects in WT and macroH2A1.2^{-/-} MEFs in the presence or absence of siRNA-mediated depletion of macroH2A1.1, Lig3, or Polq or when Parp1 was transiently inhibited upon release into mitosis. Inactivation of either of these factors was sufficient to restore the frequency of macroH2A1.2-loss-associated anaphase defects back to WT levels (Figures 4A, 4B, and S4A). A similar rescue was observed when using etoposide to increase DSB formation during mitotic progression (Figure S4B). Moreover, the frequency of anaphase aberrations in MEFs from mice deficient in both macroH2A1 splice variants (Changolkar et al., 2007) was comparable to that in WT MEFs (Figure 4C).

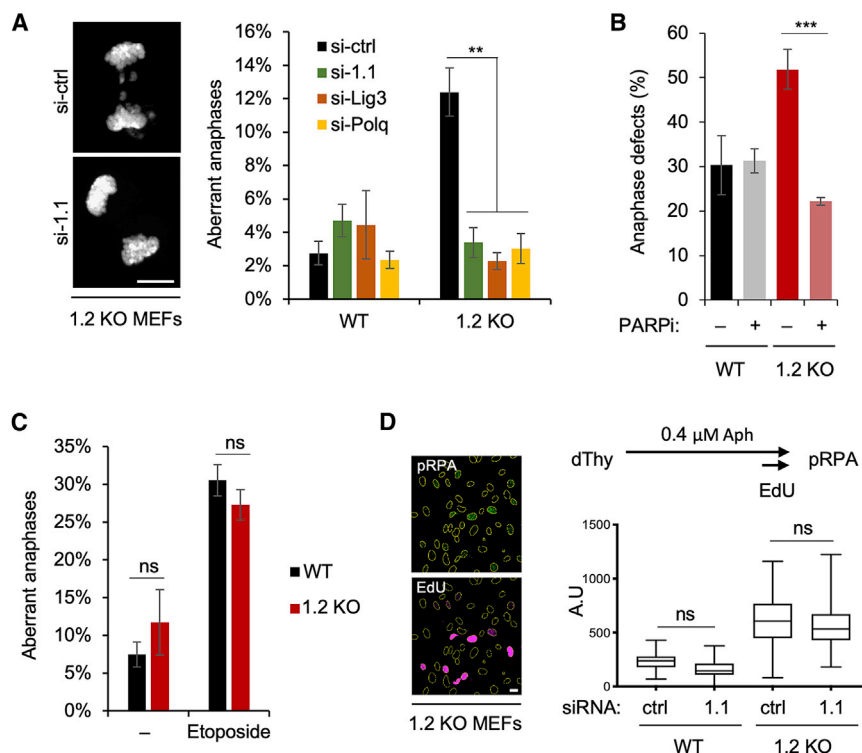


Figure 4. MacroH2A1.1 Drives Anaphase Defects via Alt-EJ upon MacroH2A1.2 Loss

(A) Anaphase aberrations in WT or macroH2A1.2 KO (1.2 KO) MEFs expressing the indicated siRNAs. Anaphases were collected as described in Figure 2A in the absence of etoposide. Values represent mean and SD ($n = 3$ replicates), and at least 40 anaphases were analyzed per replicate and sample. Scale bar, 10 μ m.

(B) Fraction of anaphase aberrations in etoposide-treated WT and macroH2A1.2 KO MEFs in the presence or absence of PARPi. Values represent mean and SD ($n = 3$ replicates, > 60 metaphases per replicate). (A and B) $**p < 0.01$ and $***p < 0.001$, based on Student's two-tailed t test.

(C) Fraction of anaphase aberrations in MEFs from macroH2A1 KO mice (Changolkar et al., 2007) in the presence or absence of etoposide. Values are expressed as mean and SD ($n = 3$ replicates, >50 metaphases per replicate). ns, not significant.

(D) pRPA intensity in EdU⁺ MEFs. Representative images are shown. Scale bar, 20 μ m. ns, not significant based on ANOVA with multiple comparison assuming non-Gaussian distribution. See also Figure S4.

To rule out that macroH2A1.1 depletion altered the macroH2A1.2-loss-associated increase in RS, and hence the source of the G2/M lesions that underlie mitotic aberrations, we assessed RS levels in the presence or absence of each macroH2A1 variant. RNA-interference-mediated macroH2A1.1 depletion was performed in WT and macroH2A1.2 KO MEFs in the presence of aphidicolin (Figure 4D). S phase cells were identified based on 5-Ethynyl-2'-deoxyuridine (EdU) incorporation, and RS was measured using RPA32 phosphorylation as a readout (Maréchal and Zou, 2015). Consistent with our previous work (Kim et al., 2018), macroH2A1.2 loss resulted in a pronounced increase in RS. MacroH2A1.1 depletion, on the other hand, did not induce RPA phosphorylation in WT cells and did not further increase RS in macroH2A1.2 KO cells. Taken together, these data point to a dual role of macroH2A1.2 in preventing chromosome segregation defects: (1) the suppression of excessive RS (Kim et al., 2018) (Figure 4D) and (2) the prevention of aberrant alt-EJ of mitotic DSBs (Figures 4A–4C). While RS is unaffected by the presence or absence of macroH2A1.1, alt-EJ depends on expression of the alternative splice variant.

MacroH2A1 Splice Variants Modulate Alt-EJ Efficiency in Tumor Cells

Providing a physiological context for macroH2A1 splice variant imbalance, previous reports demonstrated aberrant macroH2A1 alternative splicing in tumor tissue, often resulting in predominant macroH2A1.2 variant expression (Cantariño et al., 2013; Novikov et al., 2011). More recently, we reported an RS-protective role for macroH2A1.2 across fragile regions genome-wide that was particularly apparent in a rapidly dividing tumor cell

line (Kim et al., 2018). In agreement with the latter, increased genome instability triggered by the absence of macroH2A1.2 was not strictly limited to the X chromosome (Figure 2F). Together, these findings point to a broader role for macroH2A1 alternative splicing as a modulator of genome maintenance, particularly in cancer cells. In agreement with reports in tumor tissue (Cantariño et al., 2013; Novikov et al., 2011), the NCI-60 panel of cancer cell lines exhibits predominant macroH2A1.2 variant expression, with a mean abundance of 78% of total macroH2A1, ranging from 30% to 98% (Figure 5A). The NCI-60 panel thus allowed us to examine if macroH2A1 splice variant expression has predictive value for DSB repair pathway choice in a cancer setting.

Gene expression correlation analysis of well-defined HR/RS- or EJ-associated repair factors with either macroH2A1 splice variant was performed using the CellMinerCDB tool (<https://discover.nci.nih.gov/cellminerfdb>) (Rajapakse et al., 2018). Consistent with the role of macroH2A1.2 in homology-directed DSB repair (Khurana et al., 2014; Kim et al., 2018, 2019), we uncovered a strong correlation between macroH2A1.2 and HR/RS-protective repair factors (Figures 5B, S4C, and S2D). In contrast, macroH2A1.1 expression was neither indicative of HR / RS nor most canonical EJ components across NCI-60 cell lines. Instead, macroH2A1.1 positively correlated with two alt-EJ components, LIG3 and XRCC1, indicative of a link between macroH2A1.1 expression and alt-EJ in cancer cells (Figures 5B, 5C, and S4D). To experimentally test the latter, we measured alt-EJ efficiency in two NCI-60 breast cancer cell lines that express either high (Hs-578T) or low macroH2A1.1 levels (MCF7) and reciprocal macroH2A1.2 levels (Figure 5D). Confirming our

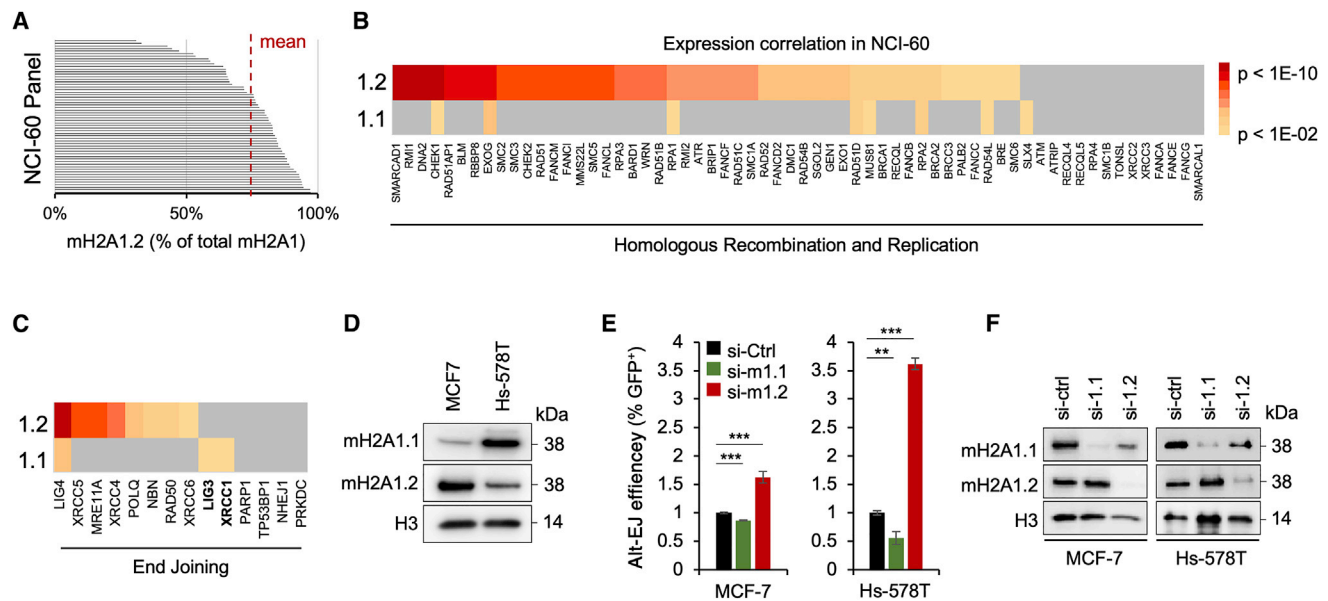


Figure 5. MacroH2A1 Variants Indicate DSB Repair Pathway Choice in Tumor Cells

(A) Relative abundance of macroH2A1.2 splice variant expression in NCI60 tumor cell lines based on RNA sequencing (RNA-seq) expression analysis in CellMinerCDB.

(B and C) Correlation of macroH2A1 splice variant expression with genes involved in genome maintenance pathways across NCI-60 tumor cell lines. Genes associated with HR and replication pathways (B) or EJ pathways (C) are shown. Heatmaps represent p values of the expression correlation, significance was assessed by two-tailed Z test.

(D) Western blot using two NCI60 cell lines with high or low macroH2A1.1 or macroH2A1.2 levels.

(E) Relative efficiency of alt-EJ in MCF-7 and Hs-578T cells with knockdown of macroH2A1.1 or macroH2A1.2. **p < 0.01 and ***p < 0.001, based on Student's two-tailed t test.

(F) Western blot showing siRNA-mediated knockdown of macroH2A1.1 and macroH2A1.2 cells from (E).

See also [Figure S4](#).

findings in U2OS cells, macroH2A1.1 depletion by siRNA resulted in a reduction in alt-EJ reporter activity in both NCI-60 cell lines, whereas macroH2A1.2 knockdown significantly increased alt-EJ ([Figures 5E and 5F](#)). Of note, the extent to which alt-EJ changed upon macroH2A1 variant manipulation correlated with the overall abundance of macroH2A1.1. Together, these findings are in agreement with our mechanistic studies in MEFs and point to a broader role for macroH2A1 splice variants as predictive markers for DNA repair pathway choice.

DISCUSSION

Providing a long elusive rationale for macroH2A1.2 enrichment on the Xi, we demonstrate here that macroH2A1.2 loss impairs Xi genome maintenance and female survival. We further define opposing roles for macroH2A1 splice variants in the regulation of DSB repair and show that genomic integrity of the Xi depends on a balanced expression of both variants ([Figure S4E](#)). In contrast with the function of macroH2A1.2 during HR and RS, our data demonstrate that macroH2A1.1 acts as a chromatin effector of alt-EJ, which mediates aberrant DSB joining and anaphase aberrations when macroH2A1.2 is absent. Underlining broader physiological relevance, we find that differential modulation of DSB repair by macroH2A1 splice variants extends from healthy to cancer cells.

The female-biased lethality observed in macroH2A1.2-deficient mice is in agreement with a recent report demonstrating that RS can trigger an excessive inflammatory response, which is preferentially lethal to female embryos. Inflammation was linked to the accumulation of micronuclei and was in part facilitated by the absence of the anti-inflammatory properties of testosterone ([McNairn et al., 2019](#)). Together with our findings, this suggests that female viability in macroH2A1.2^{-/-} mice is adversely affected by a combination of increased genome instability and micronuclei formation at the Xi and an overall exacerbated inflammatory response of female mice to genomic damage.

Underlining the central role for aberrant genome maintenance as a driver for the adverse physiological consequences of macroH2A1.2 loss, inactivation of alt-EJ is sufficient to rescue macroH2A1.2-loss-induced anaphase defects. Similarly, co-depletion of macroH2A1.1 restored Xi genome instability and female-biased lethality. While increased RS persists in the absence of both macroH2A1 variants ([Figure 4D](#)), alt-EJ of the resulting DNA lesions cannot efficiently occur without macroH2A1.1, preventing chromosome fusions and subsequent anaphase bridges. How DNA breaks are repaired when alt-EJ is impaired remains to be fully determined, but cellular mechanisms exist that tether mitotic DNA breaks until more faithful repair pathways are reactivated in the subsequent cell cycle

(Bakhomou et al., 2017; Leimbacher et al., 2019; Spies et al., 2019). It is, however, noteworthy that MEFs deficient in both macroH2A1 variants showed a trend toward increased chromosomal aberrations (Figure 4C), which raises the possibility that a lack of both variants may result in measurable and potentially harmful chromosomal defects over time. Future studies are needed to address the impact of macroH2A1 variant loss on tumorigenesis and age-associated genome instability.

While our observations explain Xi enrichment of the RS-protective macroH2A1.2 variant, the physiological relevance of macroH2A1.1 on the Xi remains to be further investigated. It is tempting to speculate that macroH2A1.1 may help to modulate PARP1 function beyond alt-EJ, given that PARP enzymes have Xi-specific roles in both genome maintenance and XCI (Ménissier de Murcia et al., 2003; Nusinow et al., 2007). Independent of its genomic location, macroH2A1.1-rich chromatin is furthermore an important regulator of mitochondrial respiration via its ability to modulate nuclear NAD⁺ consumption (Posavec Marjanović et al., 2017). In addition, the macroH2A1.1 interactors LIG3, TDP1, and PARP1 are central mediators of DNA base excision repair (BER) of single-stranded DNA lesions (Plo et al., 2003; Tomkinson et al., 2001), raising the possibility that macroH2A1.1 may also play a role in BER. However, more work is needed to investigate this possibility. Importantly, given that BER has not been implicated in the repair of etoposide-induced DNA lesions (Pommier et al., 2016), and that we are able to rescue macroH2A1.2 loss-associated mitotic defects by depleting the alt-EJ effector Polq, our findings strongly support the notion that the adverse effect of macroH2A1.1 on anaphase integrity involves alt-EJ rather than the BER pathway. It is worth noting that Polq depletion was recently found to sensitize cells to RS through a mechanism that remains to be fully determined (Wang et al., 2019). As such, Polq depletion may aggravate the impact of macroH2A1.2 loss with regard to S-phase-associated DNA damage while nevertheless protecting from subsequent alt-EJ-associated anaphase aberrations.

Although macroH2A1.1 accumulation may come at the cost of an alt-EJ permissive chromatin environment, the latter is generally counterbalanced by the presence of macroH2A1.2. Moreover, macroH2A1.1 expression correlates with cellular differentiation and proliferative arrest (Chen et al., 2015; Gaspar-Maia et al., 2013; Wan et al., 2017). As a result, cells with high macroH2A1.1 levels are less likely to undergo mitosis and concomitant alt-EJ-associated anaphase defects, while alt-EJ proficiency may provide an important backup DSB repair pathway in G1, where HR is unavailable.

Supporting the physiological relevance of our findings, the macroH2A1 alternative splicing outcome changes during cellular or developmental transitions, which is particularly well documented for malignant transformation and progression (Dardenne et al., 2012; Novikov et al., 2011). Consistent with its RS-protective role, macroH2A1.2 supports proliferation of both primary and tumor cells (Kim et al., 2018, 2019), whereas macroH2A1.1 expression negatively correlates with tumor growth (Chen et al., 2015; Paziienza et al., 2016; Sporn et al., 2009; Wan et al., 2017). Our findings in a panel of 60 tumor cell lines now point to macroH2A1 splice variant abundance as a pathologically relevant indicator of repair outcome and pathway choice

in cancer cells. We anticipate that the assessment and/or manipulation of macroH2A1 splice variant abundance, as well as a better understanding of what determines their unique protein interactomes, may provide novel strategies to manipulate genome maintenance and therapeutic outcome during malignant growth.

STAR★METHODS

Detailed methods are provided in the online version of this paper and include the following:

- KEY RESOURCES TABLE
- RESOURCE AVAILABILITY
 - Lead Contact
 - Materials Availability
 - Data and Code Availability
- EXPERIMENTAL MODEL AND SUBJECT DETAILS
 - macroH2A1.2^{-/-} mice
 - Cell Lines
- METHOD DETAILS
 - macroH2A1.2 gene targeting
 - Isolation of tail fibroblasts, embryonic fibroblasts and PBMCs
 - Cell line generation and treatments
 - Alternative end-joining (alt-EJ) and canonical NHEJ (cNHEJ) assays
 - Cell cycle analyses
 - RNA isolation and RT-PCR
 - Antibodies
 - Immunostaining and imaging
 - Anaphase analyses and micronuclei detection
 - DNA FISH
 - RNA-FISH and analyses
 - Xist segmentation analyses
 - Spectral Karyotyping
 - Cellular extract preparation and immunoblotting
 - Co-immunoprecipitation
 - Digestion and dimethyl labeling of affinity purified protein complex
 - Mass Spectrometry acquisition and data analysis
- QUANTIFICATION AND STATISTICAL ANALYSIS
 - Splice variant correlation analysis in NCI-60 cells
 - Statistical analyses

SUPPLEMENTAL INFORMATION

Supplemental Information can be found online at <https://doi.org/10.1016/j.molcel.2020.06.028>.

ACKNOWLEDGMENTS

We thank A. Nussenzweig for critical reading of the manuscript; S. Kozlov, K. Plath, K. Rajewsky, and J. Stark for reagents; T. Karpova for imaging support; S. Das and T. Andresson for MS analyses; E. Southon and the Mouse Cancer Genetics Program at NCI-Frederick for gene targeting and ESC injection; and the Biowulf, High-Performance Computing Group, Center for Information Technology (CIT), NIH for their computational support. High-throughput imaging work was performed at the High-Throughput Imaging Facility (HiTIF)/Center for Cancer Research/National Cancer Institute/NIH. This work was supported by a grant from the Daiichi Sankyo Foundation of Life Science

(Japan) to E.H. and the Intramural Research Program of the National Institutes of Health (NIH), National Cancer Institute (NCI), Center for Cancer Research (grants Z01 BC006150 to Y.P., ZIA BC010411 to M.I.A., and ZIA BC011283 to P.O.).

AUTHOR CONTRIBUTIONS

R.S., E.K.H., and P.O. designed experiments; E.K.H. performed colP analyses; A.D.T. and P.O. designed and cloned the ESC targeting vector; S.B. performed spectral karyotype (SKY) analyses and DNA-FISH in PBMCs; and R.S. performed all other experiments with help from E.S. D.M.S. performed statistical analyses and provided bioinformatics support. W.C.R. performed CellminerCDB analyses with help from Y.P. and M.I.A. P.O. and R.S. wrote the paper with insights from all co-authors.

DECLARATION OF INTERESTS

The authors declare no competing interests.

Received: September 19, 2019

Revised: April 24, 2020

Accepted: June 17, 2020

Published: July 9, 2020

REFERENCES

- Ait Saada, A., Teixeira-Silva, A., Iraqui, I., Costes, A., Hardy, J., Paoletti, G., Freon, K., and Lambert, S.A.E. (2017). Unprotected replication forks are converted into mitotic sister chromatid bridges. *Mol. Cell* 66, 398–410.e394.
- Bakhom, S.F., Kabeche, L., Compton, D.A., Powell, S.N., and Bastians, H. (2017). Mitotic DNA damage response: at the crossroads of structural and numerical cancer chromosome instabilities. *Trends Cancer* 3, 225–234.
- Bennardo, N., Cheng, A., Huang, N., and Stark, J.M. (2008). Alternative-NHEJ is a mechanistically distinct pathway of mammalian chromosome break repair. *PLoS Genet.* 4, e1000110.
- Berthold, M.R., Cebon, N., Dill, F., Gabriel, T.R., Kotter, T., Meinel, T., Ohl, P., Sieb, C., Thiel, K., and Wiswedel, B. (2008). KNIME: the Konstanz information miner. *Stud. Class Data Anal.* 319–326.
- Burrell, R.A., McClelland, S.E., Endesfelder, D., Groth, P., Weller, M.C., Shaikh, N., Domingo, E., Kanu, N., Dewhurst, S.M., Gronroos, E., et al. (2013). Replication stress links structural and numerical cancer chromosomal instability. *Nature* 494, 492–496.
- Cantariño, N., Douet, J., and Buschbeck, M. (2013). MacroH2A—an epigenetic regulator of cancer. *Cancer Lett.* 336, 247–252.
- Ceccaldi, R., Liu, J.C., Amunugama, R., Hajdu, I., Primack, B., Petalcorin, M.I., O'Connor, K.W., Konstantinopoulos, P.A., Elledge, S.J., Boulton, S.J., et al. (2015). Homologous-recombination-deficient tumours are dependent on Polθ-mediated repair. *Nature* 518, 258–262.
- Changolkar, L.N., Costanzi, C., Leu, N.A., Chen, D., McLaughlin, K.J., and Pehrson, J.R. (2007). Developmental changes in histone macroH2A1-mediated gene regulation. *Mol. Cell Biol.* 27, 2758–2764.
- Chen, H., Ruiz, P.D., McKimpson, W.M., Novikov, L., Kitsis, R.N., and Gamble, M.J. (2015). MacroH2A1 and ATM play opposing roles in paracrine senescence and the senescence-associated secretory phenotype. *Mol. Cell* 59, 719–731.
- Costanzi, C., and Pehrson, J.R. (1998). Histone macroH2A1 is concentrated in the inactive X chromosome of female mammals. *Nature* 393, 599–601.
- Dabin, J., Fortuny, A., and Polo, S.E. (2016). Epigenome maintenance in response to DNA damage. *Mol. Cell* 62, 712–727.
- Dardenne, E., Pierredon, S., Driouch, K., Gratadou, L., Lacroix-Triki, M., Espinoza, M.P., Zonta, E., Germann, S., Mortada, H., Villemin, J.P., et al. (2012). Splicing switch of an epigenetic regulator by RNA helicases promotes tumor-cell invasiveness. *Nat. Struct. Mol. Biol.* 19, 1139–1146.
- Das, S., Bosley, A.D., Ye, X., Chan, K.C., Chu, I., Green, J.E., Issaq, H.J., Veenstra, T.D., and Andresson, T. (2010). Comparison of strong cation exchange and SDS-PAGE fractionation for analysis of multiprotein complexes. *J. Proteome Res.* 9, 6696–6704.
- Deng, L., Wu, R.A., Sonnevile, R., Kochenova, O.V., Labib, K., Pellman, D., and Walter, J.C. (2019). Mitotic CDK promotes replisome disassembly, fork breakage, and complex DNA rearrangements. *Mol. Cell* 73, 915–929.e916.
- Dietz, C., and Berthold, M.R. (2016). KNIME for open-source bioimage analysis: a tutorial. *Adv. Anat. Embryol. Cell Biol.* 219, 179–197.
- Downes, C.S., Clarke, D.J., Mullinger, A.M., Giménez-Abián, J.F., Creighton, A.M., and Johnson, R.T. (1994). A topoisomerase II-dependent G2 cycle checkpoint in mammalian cells/. *Nature* 372, 467–470.
- Durkin, M.E., Qian, X., Popescu, N.C., and Lowy, D.R. (2013). Isolation of mouse embryo fibroblasts. *Biol. Protoc.* 3, e908.
- Engreitz, J.M., Pandya-Jones, A., McDonel, P., Shishkin, A., Sirokman, K., Surka, C., Kadri, S., Xing, J., Goren, A., Lander, E.S., et al. (2013). The Xist lncRNA exploits three-dimensional genome architecture to spread across the X chromosome. *Science* 341, 1237973.
- Gaspar-Maia, A., Qadeer, Z.A., Hasson, D., Ratnakumar, K., Leu, N.A., Leroy, G., Liu, S., Costanzi, C., Valle-Garcia, D., Schaniel, C., et al. (2013). MacroH2A histone variants act as a barrier upon reprogramming towards pluripotency. *Nat. Commun.* 4, 1565.
- Gibson, B.A., Zhang, Y., Jiang, H., Hussey, K.M., Shrimp, J.H., Lin, H., Schwede, F., Yu, Y., and Kraus, W.L. (2016). Chemical genetic discovery of PARP targets reveals a role for PARP-1 in transcription elongation. *Science* 353, 45–50.
- Gostissa, M., Alt, F.W., and Chiarle, R. (2011). Mechanisms that promote and suppress chromosomal translocations in lymphocytes. *Annu. Rev. Immunol.* 29, 319–350.
- Jäger, N., Schlesner, M., Jones, D.T., Raffel, S., Malm, J.P., Junge, K.M., Weichenhan, D., Bauer, T., Ishaque, N., Kool, M., et al. (2013). Hypermethylation of the inactive X chromosome is a frequent event in cancer. *Cell* 155, 567–581.
- Jonkers, I., Monkhorst, K., Rentmeester, E., Grootegoed, J.A., Grosveld, F., and Gribnau, J. (2008). Xist RNA is confined to the nuclear territory of the silenced X chromosome throughout the cell cycle. *Mol. Cell Biol.* 28, 5583–5594.
- Jowhar, Z., Shachar, S., Gudla, P.R., Wangsa, D., Torres, E., Russ, J.L., Pegoraro, G., Ried, T., Raznahan, A., and Misteli, T. (2018). Effects of human sex chromosome dosage on spatial chromosome organization. *Mol. Cell Biol.* 29, 2458–2469.
- Jungmichel, S., Rosenthal, F., Altmeyer, M., Lukas, J., Hottiger, M.O., and Nielsen, M.L. (2013). Proteome-wide identification of poly(ADP-Ribosylation) targets in different genotoxic stress responses. *Mol. Cell* 52, 272–285.
- Khurana, S., Kruhlak, M.J., Kim, J., Tran, A.D., Liu, J., Nyswaner, K., Shi, L., Jailwala, P., Sung, M.H., Hakim, O., and Oberdoerffer, P. (2014). A macrohistone variant links dynamic chromatin compaction to BRCA1-dependent genome maintenance. *Cell Rep.* 8, 1049–1062.
- Kim, B.J., Chan, D.W., Jung, S.Y., Chen, Y., Qin, J., and Wang, Y. (2017). The histone variant MacroH2A1 is a BRCA1 ubiquitin ligase substrate. *Cell Rep.* 19, 1758–1766.
- Kim, J., Sturgill, D., Sebastian, R., Khurana, S., Tran, A.D., Edwards, G.B., Kruswick, A., Burkett, S., Hosogane, E.K., Hannon, W.W., et al. (2018). Replication stress shapes a protective chromatin environment across fragile genomic regions. *Mol. Cell* 69, 36–47.e37.
- Kim, J., Sun, C., Tran, A.D., Chin, P.J., Ruiz, P.D., Wang, K., Gibbons, R.J., Gamble, M.J., Liu, Y., and Oberdoerffer, P. (2019). The macroH2A1.2 histone variant links ATRX loss to alternative telomere lengthening. *Nat. Struct. Mol. Biol.* 26, 213–219.
- Koren, A., and McCarroll, S.A. (2014). Random replication of the inactive X chromosome. *Genome Res.* 24, 64–69.
- Kustatscher, G., Hothorn, M., Pugieux, C., Scheffzek, K., and Ladurner, A.G. (2005). Splicing regulates NAD metabolite binding to histone macroH2A. *Nat. Struct. Mol. Biol.* 12, 624–625.

- Lee, D.H., Acharya, S.S., Kwon, M., Drane, P., Guan, Y., Adelmant, G., Kalev, P., Shah, J., Pellman, D., Marto, J.A., and Chowdhury, D. (2014). Dephosphorylation enables the recruitment of 53BP1 to double-strand DNA breaks. *Mol. Cell* *54*, 512–525.
- Leimbacher, P.A., Jones, S.E., Shorrocks, A.K., de Marco Zompit, M., Day, M., Blaauwendraad, J., Bundschuh, D., Bonham, S., Fischer, R., Fink, D., et al. (2019). MDC1 interacts with TOPBP1 to maintain chromosomal stability during mitosis. *Mol. Cell* *74*, 571–583.e578.
- Lewandoski, M., Meyers, E.N., and Martin, G.R. (1997). Analysis of Fgf8 gene function in vertebrate development. *Cold Spring Harb. Symp. Quant. Biol.* *62*, 159–168.
- Machiela, M.J., Zhou, W., Karlins, E., Sampson, J.N., Freedman, N.D., Yang, Q., Hicks, B., Dagnall, C., Hautman, C., Jacobs, K.B., et al. (2016). Female chromosome X mosaicism is age-related and preferentially affects the inactivated X chromosome. *Nat. Commun.* *7*, 11843.
- Maréchal, A., and Zou, L. (2015). RPA-coated single-stranded DNA as a platform for post-translational modifications in the DNA damage response. *Cell Res.* *25*, 9–23.
- Mateos-Gomez, P.A., Gong, F., Nair, N., Miller, K.M., Lazzerini-Denchi, E., and Sfeir, A. (2015). Mammalian polymerase θ promotes alternative NHEJ and suppresses recombination. *Nature* *518*, 254–257.
- McNairn, A.J., Chuang, C.H., Bloom, J.C., Wallace, M.D., and Schimenti, J.C. (2019). Female-biased embryonic death from inflammation induced by genomic instability. *Nature* *567*, 105–108.
- Ménissier de Murcia, J., Ricoul, M., Tartier, L., Niedergang, C., Huber, A., Dantzer, F., Schreiber, V., Amé, J.C., Dierich, A., LeMeur, M., et al. (2003). Functional interaction between PARP-1 and PARP-2 in chromosome stability and embryonic development in mouse. *EMBO J.* *22*, 2255–2263.
- Minocherhomji, S., Ying, S., Bjerregaard, V.A., Bursomanno, S., Aleliunaite, A., Wu, W., Mankouri, H.W., Shen, H., Liu, Y., and Hickson, I.D. (2015). Replication stress activates DNA repair synthesis in mitosis. *Nature* *528*, 286–290.
- Nesbitt, M.N., and Francke, U. (1973). A system of nomenclature for band patterns of mouse chromosomes. *Chromosoma* *41*, 145–158.
- Novikov, L., Park, J.W., Chen, H., Klerman, H., Jalloh, A.S., and Gamble, M.J. (2011). QKI-mediated alternative splicing of the histone variant MacroH2A1 regulates cancer cell proliferation. *Mol. Cell Biol.* *31*, 4244–4255.
- Nusinow, D.A., Hernández-Muñoz, I., Fazio, T.G., Shah, G.M., Kraus, W.L., and Panning, B. (2007). Poly(ADP-ribose) polymerase 1 is inhibited by a histone H2A variant, MacroH2A, and contributes to silencing of the inactive X chromosome. *J. Biol. Chem.* *282*, 12851–12859.
- Olivo-Marin, J.C. (2002). Extraction of spots in biological images using multi-scale products. *Pattern Recognit.* *35*, 1989–1996.
- Orthwein, A., Fradet-Turcotte, A., Noordermeer, S.M., Canny, M.D., Brun, C.M., Strecker, J., Escribano-Diaz, C., and Durocher, D. (2014). Mitosis inhibits DNA double-strand break repair to guard against telomere fusions. *Science* *344*, 189–193.
- Ouararhni, K., Hadj-Slimane, R., Ait-Si-Ali, S., Robin, P., Mietton, F., Harel-Bellan, A., Dimitrov, S., and Hamiche, A. (2006). The histone variant mH2A1.1 interferes with transcription by down-regulating PARP-1 enzymatic activity. *Genes Dev.* *20*, 3324–3336.
- Pazienza, V., Panebianco, C., Rappa, F., Memoli, D., Borghesan, M., Cannito, S., Oji, A., Mazza, G., Tamburrino, D., Fusai, G., et al. (2016). Histone macroH2A1.2 promotes metabolic health and leanness by inhibiting adipogenesis. *Epigenetics Chromatin* *9*, 45.
- Plath, K., Fang, J., Mlynarczyk-Evans, S.K., Cao, R., Worringer, K.A., Wang, H., de la Cruz, C.C., Otte, A.P., Panning, B., and Zhang, Y. (2003). Role of histone H3 lysine 27 methylation in X inactivation. *Science* *300*, 131–135.
- Plo, I., Liao, Z.Y., Barceló, J.M., Kohlhagen, G., Caldecott, K.W., Weinfeld, M., and Pommier, Y. (2003). Association of XRCC1 and tyrosyl DNA phosphodiesterase (Tdp1) for the repair of topoisomerase I-mediated DNA lesions. *DNA Repair (Amst.)* *2*, 1087–1100.
- Pommier, Y., Sun, Y., Huang, S.N., and Nitiss, J.L. (2016). Roles of eukaryotic topoisomerases in transcription, replication and genomic stability. *Nat. Rev. Mol. Cell Biol.* *17*, 703–721.
- Posavec Marjanović, M., Hurtado-Bagès, S., Lassi, M., Valero, V., Malinverni, R., Delage, H., Navarro, M., Corujo, D., Guberovic, I., Douet, J., et al. (2017). MacroH2A1.1 regulates mitochondrial respiration by limiting nuclear NAD⁺ consumption. *Nat. Struct. Mol. Biol.* *24*, 902–910.
- Rajapakse, V.N., Luna, A., Yamade, M., Loman, L., Varma, S., Sunshine, M., Iorio, F., Sousa, F.G., Elloumi, F., Aladjem, M.I., et al. (2018). CellMinerCDB for integrative cross-database genomics and pharmacogenomics analyses of cancer cell lines. *iScience* *10*, 247–264.
- Russell, L.M., Strike, P., Browne, C.E., and Jacobs, P.A. (2007). X chromosome loss and ageing. *Cytogenet. Genome Res.* *116*, 181–185.
- Spies, J., Lukas, C., Somyajit, K., Rask, M.B., Lukas, J., and Neelsen, K.J. (2019). 53BP1 nuclear bodies enforce replication timing at under-replicated DNA to limit heritable DNA damage. *Nat. Cell Biol.* *21*, 487–497.
- Sporn, J.C., Kustatscher, G., Hothorn, T., Collado, M., Serrano, M., Muley, T., Schnabel, P., and Ladurner, A.G. (2009). Histone macroH2A isoforms predict the risk of lung cancer recurrence. *Oncogene* *28*, 3423–3428.
- Telenius, H., Carter, N.P., Bebb, C.E., Nordenskjöld, M., Ponder, B.A., and Tunnacliffe, A. (1992). Degenerate oligonucleotide-primed PCR: general amplification of target DNA by a single degenerate primer. *Genomics* *13*, 718–725.
- Timinszky, G., Till, S., Hassa, P.O., Hothorn, M., Kustatscher, G., Nijmeijer, B., Colombelli, J., Altmeyer, M., Stelzer, E.H., Scheffzek, K., et al. (2009). A macrodomain-containing histone rearranges chromatin upon sensing PARP1 activation. *Nat. Struct. Mol. Biol.* *16*, 923–929.
- Tomkinson, A.E., Chen, L., Dong, Z., Leppard, J.B., Levin, D.S., Mackey, Z.B., and Motycka, T.A. (2001). Completion of base excision repair by mammalian DNA ligases. *Prog. Nucleic Acid Res. Mol. Biol.* *68*, 151–164.
- Wan, D., Liu, C., Sun, Y., Wang, W., Huang, K., and Zheng, L. (2017). MacroH2A1.1 cooperates with EZH2 to promote adipogenesis by regulating Wnt signaling. *J. Mol. Cell Biol.* *9*, 325–337.
- Wang, Z., Song, Y., Li, S., Kurian, S., Xiang, R., Chiba, T., and Wu, X. (2019). DNA polymerase θ (POLQ) is important for repair of DNA double-strand breaks caused by fork collapse. *J. Biol. Chem.* *294*, 3909–3919.

STAR★METHODS

KEY RESOURCES TABLE

REAGENT or RESOURCE	SOURCE	IDENTIFIER
Antibodies		
α -macroH2A1.2	Millipore	Cat#MABE61, RRID:AB_10807977
α -macroH2A1.1	Cell Signaling Technologies	Cat#12455, RRID:AB_2797923
α -Lig3	GeneTex	Cat#GTX103172, RRID:AB_2036773
α -FLAG	Agilent	Cat#200472, RRID:AB_10596649
α -PCNA	Santa Cruz	Cat#sc-56, RRID:AB_628110
α -H2B	Abcam	Cat#ab1790, RRID:AB_302612
α -GAPDH	Santa Cruz	Cat#sc-32233, RRID:AB_627679
α -PARP1	Cell Signaling Technologies	Cat#9542, RRID:AB_2160739
α -H3	Cell Signaling Technologies	Cat#9715, RRID:AB_331563
α -centromere	Antibodies incorporated	Cat#15-234-0001, RRID:AB_2687472
α -PAR	Trevigen	Cat#4335-MC-100, RRID:AB_2572318
α -H3K27me3	Abcam	Cat#ab6002, RRID:AB_305237
α -phosphor RPA32 (Ser4 / Ser8)	Bethyl	Cat#A300-245A, RRID:AB_210547
Goat anti-mouse IgG-HRP	Santa Cruz	Cat#sc-2005, RRID:AB_631736
Goat anti-rabbit IgG-HRP	Santa Cruz	Cat#sc-2004, RRID:AB_631746
Chemicals, Peptides, and Recombinant Proteins		
Aphidicolin	Sigma	Cat#A0781
EdU (5-ethynyl-2'-deoxyuridine)	ThermoFisher Scientific	Cat#E10187
Alexa Fluor 647-azide	ThermoFisher Scientific	Cat#A10277
Hoechst 33342	ThermoFisher Scientific	Cat#H3570
RO3306	Selleckchem	Cat#S7747
Alexa Fluor 488-5-dUTP	ThermoFisher Scientific	Cat#C11397
Anti-FLAG M2 Magnetic beads	Sigma	Cat#M8823
Veliparib (PARPi)	Selleckchem	Cat#S1004
Puromycin	Sigma	Cat#P8833
Collagenase II	ThermoFisher Scientific	Cat#17101015
Phytohaemagglutinin	Sigma	Cat#L1668
PI/RNase staining buffer	BD PharMingen	Cat#550825
cOmplete Mini EDTA-free protease inhibitor	Roche	Cat#11836170001
KaryoMAX Colcemid	ThermoFisher Scientific	Cat#15210-040
mLIF	ThermoFisher Scientific	Cat#PMC9484
Doxycycline	Sigma	Cat#D9891
All-trans retinoic acid	Sigma	Cat#R2625
Critical Commercial Assays		
Click-iT EdU Alexa Fluor 647 Imaging Kit	ThermoFisher Scientific	Cat#C10340
Phosphatase inhibitor cocktail set II	Millipore	Cat#524625
SuperscriptIII	ThermoFisher Scientific	Cat#18080044
TURBO DNase	ThermoFisher Scientific	Cat#AM1907
Lipofectamine 2000	ThermoFisher Scientific	Cat#11668
CGH Bioprime array kit	ThermoFisher Scientific	Cat#18095011
Histone H3 (phospho S10) assay kit	Abcam	Cat#ab115127
21-color mouse SKY paint kit	Applied spectral imaging	Cat#FPRPR0030

(Continued on next page)

Continued

REAGENT or RESOURCE	SOURCE	IDENTIFIER
Deposited Data		
Mass spectrometry analyses, see Table S1	This study	MassIVE: MSV000085351
Experimental Models: Cell Lines		
BJ	ATCC	Cat#CRL-2522, RRID:CVCL_3653
IMR-90	Coriell	Cat#190-15, RRID:CVCL_0347
T-REx-293 Cell Line	Thermo Fisher Scientific	Cat#R78007, RRID:CVCL_U427
FLAG-macroH2A1.1 (in HEK293 T-REx)	This study	N/A
FLAG-macroH2A1.2 (in HEK293 T-REx)	This study	N/A
MCF-7	ATCC	Cat#HTB-22, RRID:CVCL_0031
Hs 578T	ATCC	Cat#HTB-126, RRID:CVCL_0332
pEJ5 U2OS (cNHEJ)	Gift from Jeremy Stark	N/A
pEJ2 U2OS (alt-EJ)	Gift from Jeremy Stark	N/A
C57BL/6 Bruce4 ES cells	Lewandoski et al., 1997	N/A
MS2-Xist female ES cells	Jonkers et al., 2008	N/A
pSM33 male ES cells	Engreitz et al., 2013	N/A
macroH2A1.2 WT and KO MEFs	This study	N/A
Tail fibroblasts from WT and KO mice	This study	N/A
Experimental Models: Organisms/Strains		
MacroH2A1.2 KO mice	This study	NCI Mouse Repository, Cat#01BQO
MacroH2A1 KO mice	Changolkar et al., 2007	N/A
β -actin Cre transgenic mice	Lewandoski et al., 1997	The Jackson Laboratory, Cat#B6N.FVB-Tmem163 ^{Tg(ACTB-cre)2Mrt/CjDswJ}
Oligonucleotides		
shRNA targeting sequences, see Table S2	This study	N/A
siRNA targeting sequences, see Table S2	This study	N/A
Primers for gene targeting, see Table S3	This study	N/A
Primers for RT-PCR, see Table S3	This study	N/A
Primers for genotyping, see Table S3	This study	N/A
Recombinant DNA		
EJ2	Gift from Jeremy Stark	RRID:Addgene_44025
pCBASceI	Gift from Maria Jasin	RRID:Addgene_26477
pcDNA3-EGFP	Gift from Doug Golenbock	RRID:Addgene_13031
pEZ-Frt-lox-DT	Gift from Klaus Rajewsky	RRID:Addgene_11736
Full-length mouse Xist plasmid	Gift from Kathrin Plath	N/A
pLKO.1	Gift from David Root	RRID:Addgene_10878
Software and Algorithms		
ImageJ	NIH	https://imagej.nih.gov/ij/
FlowJo	BD Biosciences	https://www.flowjo.com
Prism	GraphPad	https://www.graphpad.com/scientific-software/prism/
Proteome Discoverer 1.4	ThermoFisher Scientific	https://www.thermofisher.com/us/en/home.html
R	R Core Team	http://www.r-project.org
KNIME	Berthold et al., 2008	https://www.knime.com/
HiFish acquisition software	GenASIs, Applied Spectral Imaging	https://spectral-imaging.com/
HiSKY 7.2	Genesis, Applied Spectral Imaging	https://spectral-imaging.com/
Spot detection algorithm	Olivo-Marin, 2002	N/A
Other		
CellMinerCDB	NIH	https://discover.nci.nih.gov/cellminerfdb/

RESOURCE AVAILABILITY

Lead Contact

Further information and requests for resources and reagents should be directed to and will be fulfilled by the Lead Contact, Philipp Oberdoerffer (Philipp.Oberdoerffer@nih.gov).

Materials Availability

- MacroH2A1.2 KO mice generated in this study have been deposited to the NCI Mouse Repository, Cat#01BQO, strain name *B6.Cg-Macroh2a1 < tm1.2Pobe > /Nci*; synonym: *B6.Cg-macroH2A1.2 KO*.
- All unique reagents generated in this study are available from the Lead Contact with a completed Materials Transfer Agreement.

Data and Code Availability

- Original/source data for [Figures 1, 2, 3, 4, and 5](#) in the paper is available [Mendeley Data: <https://doi.org/10.17632/xh2z6m4t75.1>].
- Mass spectrometry data have been deposited in MassIVE: <https://massive.ucsd.edu/ProteoSAFe/static/massive.jsp> under the identifier MassIVE: MSV000085351.

EXPERIMENTAL MODEL AND SUBJECT DETAILS

macroH2A1.2^{-/-} mice

Gene-targeted macroH2A1.2^{fl-neo/+} ES cells (see below) were injected into C57BL/6 albino (cBRD/cBRD) blastocysts and chimeric males were crossed to C57BL/6 females. macroH2A1.2^{fl-neo/+} mice were bred to β -actin Cre transgenic mice ([Lewandoski et al., 1997](#)) (backcrossed to C57BL/6 for more than 20 generations) for germline deletion of the neo^R-E6a cassette, resulting in mice heterozygous for the macroH2A1.2 KO allele (macroH2A1.2^{+/-}). The latter were interbred to generate macroH2A1.2^{-/-} mice. All animal breeding and experimentation followed guidelines approved by the National Institutes of Health Institutional Animal Care and Use Committee.

Cell Lines

Human female lung IMR90 (Coriell) and male foreskin BJ fibroblasts (ATCC) were cultured in MEM (GIBCO), supplemented with 10% (v/v) FBS (Gemini), 2 mM L-Glutamine (GIBCO), 1 mM sodium pyruvate (Sigma) and 0.1 (1X) mM Non-Essential Amino Acids (NEAA, GIBCO). Alt-EJ U2OS cells (gift from J. Stark, City of Hope) were cultured in DMEM (GIBCO) with 10% FBS. HEK293 T-REx cells (gift from The Broad Institute, Cambridge) were grown in DMEM with 10% FBS containing Blasticidin (Invivogen, 15 μ g/ml) and hygromycin B (Thermo Fisher, 100 μ g/ml). MEFs were grown in DMEM (GIBCO) containing β -mercaptoethanol and Pen/Strep (GIBCO), supplemented with 10% FBS. mTFs were grown in mTF media (1:1 DMEM and Ham's F10, 20% FBS, Non-Essential Amino Acids, Pen/Strep, β -mercaptoethanol, Sodium pyruvate, HEPES and L-Glutamine, all from GIBCO). pSM33 male ES cells ([Engreitz et al., 2013](#)) and MS2-Xist female ES cells ([Jonkers et al., 2008](#)) were a kind gift from Kathrin Plath, UCLA. ES cells were grown on mitomycin C-treated mouse embryonic fibroblasts (feeder cells) in ES cell media (Knockout DMEM (Invitrogen), 15% FBS, 2 mM L-glutamine, 100 μ M Non-Essential Amino Acids, 1% Pen/Strep, 0.1% β -mercaptoethanol, 1000 U/mL mLIF (Invitrogen)). All cells were maintained at 37°C in a humidified incubator containing 5% CO₂. Primary cells and ES cell lines were not tested for mycoplasma, all other cell lines were mycoplasma-free.

METHOD DETAILS

macroH2A1.2 gene targeting

5' and 3' arms of homology were PCR-amplified and inserted into pEZ-Frt-lox-DT (a gift from K. Rajewsky, Addgene, plasmid #11736). A 840 bp *H2AFY* exon 6a (E6a)-containing DNA fragment was PCR-amplified and inserted downstream of an Frt- and LoxP flanked neo^R gene resulting in a loxP-flanked FRT-neo^R-E6a cassette. See Table S3 for primer sequences. Gene targeting was performed in C57BL/6 Bruce4 ES cells as described previously ([Lewandoski et al., 1997](#)). Neomycin-resistant ES cells were analyzed for correct transgene integration by Southern Blot analysis, using PCR-generated 5' and 3' external probes and a 5' internal probe in combination with HindIII or BamHI digests of genomic ES cell DNA, see [Table S3](#) for primer sequences. The targeted allele is referred to as macroH2A1.2^{fl-neo}.

Isolation of tail fibroblasts, embryonic fibroblasts and PBMCs

Mouse tail fibroblasts (mTF) were prepared from 6 week-old mice. Briefly, animals were euthanized, and the tails were de-skinned. The skin was wiped in 70% ethanol and cut into small pieces (2 X 2 mm) in mTF media (see above) containing 1.6 mg/ml collagenase II (Thermo Fisher). After 24 h, a cell strainer was used to remove hair and debris. One million cells were plated onto a 10 cm dish in fresh

mTF medium and passaged when confluent. For mouse embryonic fibroblasts (MEFs), embryos from WT and KO littermates were isolated on E12.5 and processed as described previously (Durkin et al., 2013). Individual MEF strains were genotyped for sex using SRY PCR (see Table S3 for primer sequences) and stored at passage 2. For experiments, WT and KO MEFs from identical passage numbers were used, passage numbers ranged from 3-6. For PBMCs, blood samples from animals were drawn by retro-orbital bleeding and cultured in phytohaemagglutinin stimulated RPMI media (GIBCO) with 10% FBS and Pen/Strep for 48 h.

Cell line generation and treatments

Targeted, Flp-recombinase-mediated insertion of a single copy of the Flag-macroH2A1.1- or Flag-macroH2A1.2-encoding transgenes into HEK293 T-REX cells was performed as described previously (Kim et al., 2018). siRNAs were transfected using DF-1 reagent following the manufacturer's instructions (Dharmacon) and analyzed at 72 - 96 h post transfection. Lentiviral infection of LKO.1 shRNA-expression vectors was carried out by spin infection (2500 rpm, 90 min, Beckman-Coulter Allegra X-12R centrifuge) with 8 μ g/ml polybrene (Sigma). Cells were incubated overnight prior to virus removal and selection with puromycin (1 μ g/ml, Invitrogen). See Table S2 for siRNA and shRNA sequences. To induce Xist expression, pSM33 cells were plated as single cells without feeder cells on 0.1% gelatin (Millipore) coated coverslips overnight. Doxycycline (2 μ g/ml) was added subsequently for 8 h and the coverslips were processed for RNA FISH as described below. For differentiation experiments in MS2-Xist ES cells, cells were depleted of feeder cells and plated onto acid-etched, gelatin coated coverslip for 24 h in ES cell media without mLIF. Subsequently, all-trans retinoic acid (R2625, Sigma) was added and cells were allowed to differentiate for 6 days, followed by RNA FISH or RNA collection. For undifferentiated controls, feeder cell-depleted ES cells were grown on coverslips for 24 hours with mLIF containing ES media and fixed for RNA FISH or RNA collection. For G2/M arrest, cells were treated with 10 μ M CDK1 inhibitor (CDK1i) RO3306 for 16 h. For PARP inhibition, cells were treated with 10 μ M veliparib (Selleckchem), for topoisomerase II inhibition, cells were treated with 5 μ M etoposide for the indicated times. Irradiation experiments were performed using an X-ray irradiator (X-rad 320, Precision X-Ray).

Alternative end-joining (alt-EJ) and canonical NHEJ (cNHEJ) assays

Detection of alt-EJ was performed using a previously described alt-EJ U2OS reporter cell line (Bennardo et al., 2008). Briefly, cells were first transfected siRNAs on day 1. On day 2, cells were transfected with 1 μ g of I-SceI expression vector pCBASceI (Addgene #26477) or 1 μ g of pcDNA3-EGFP (Addgene #13031) using Lipofectamine 2000 (Thermo Fisher) according to the manufacturer's instructions. Where indicated, PARPi treatment was performed 24 h prior to analysis. The fraction of GFP-positive cells was assayed 72 h post siRNA transfection using a FACSCalibur (BD, USA). Values were normalized to transfection efficiency based on pcDNA3-EGFP. For experiments involving transient transfection, alt-EJ reporter plasmid (EJ2) was transfected along with I-SceI expression vector. Detection of cNHEJ was performed using a previously described cNHEJ U2OS reporter cell line (Bennardo et al., 2008).

Cell cycle analyses

For DNA content analyses, cells were fixed in 70% ethanol at -20°C overnight. Fixed cells were resuspended in propidium-iodide (PI) / RNase A staining buffer (BD PharMingen) at room temperature for 20 min. DNA content was determined by flow cytometry (FACS Calibur, BD PharMingen). For mitotic index analyses, chromatin extracts were collected 30 min after release from G2/M arrest and analyzed for H3-pS10 content using the phospho-S10 detection kit (Abcam, ab115127) following the manufacturer's instructions.

RNA isolation and RT-PCR

Total RNA was extracted using the RNeasy Mini Kit according to the manufacturer's instructions (QIAGEN). cDNA was synthesized from 0.5–1 μ g of total RNA using the Superscript III reverse transcriptase RT-PCR system (Thermo Fisher), and expression of the indicated genes was analyzed by quantitative RT-PCR using a LightCycler 480 II (Roche) (see Table S3 for primer sequences). The standard comparative cycle threshold method was used for cDNA quantification.

Antibodies

The following antibodies were used for western blot: α -macroH2A1.2 (Millipore, MABE61), α -macroH2A1.1 (CST, 12455), α -Lig3 (GeneTex, GTX103172), α -FLAG (Agilent, 200472), α -PCNA (Santa Cruz, sc-56), α -H2B (Abcam, ab1790), α -GAPDH (Santa Cruz, sc-32233), α -PARP1 (CST, 9542S), α -H3 (CST, 9715). Secondary antibodies were goat anti-mouse IgG-HRP (Santa Cruz, sc-2005) and goat anti-rabbit IgG-HRP (Santa Cruz, sc-2004). Primary antibodies for IF were: α -macroH2A1.1 (CST, 12455), α -macroH2A1.2 (Millipore, MABE61), α -centromere (Antibodies incorporated, 15-234-0001), α -PAR (Trevigen, 4335-MC-100), H3K27me3 (Abcam, ab6002), phosphor RPA32 (Ser4 / Ser8) (Bethyl, A300-245A). Secondary antibodies were from Life Technologies (goat- α -mouse, goat- α -rabbit or goat- α -human conjugated to Alexa Fluor 488 or 568).

Immunostaining and imaging

Cells were fixed and in PTEMF buffer (20 mM PIPES pH 6.8, 10 mM EGTA, 0.2% Triton X-100, 1 mM MgCl₂ and 4% paraformaldehyde) at room temperature and then permeabilized in 0.5% Triton X-100. Cells were washed and blocked for 1 h at room temperature (3% BSA, 0.5% Triton X-100 in PBS). Primary and secondary antibody stainings were carried out in 3% BSA and PBS-T. For S phase discrimination, cells were pulsed with 10 μ M EdU (Life Technologies) at 37 $^{\circ}\text{C}$, prior to fixation. Incorporated EdU was Click-labeled

using azide-linked Alexa Fluor-647 (Life Technologies). Confocal z-stacks were acquired using a Zeiss LSM 780 microscope. Images were displayed and analyzed as maximum intensity projections.

Anaphase analyses and micronuclei detection

For anaphases, MEFs were plated onto gelatin coated coverslips for 6 h followed by treatment with CDK1i. Cells were washed 3 times with pre-warmed PBS and allowed to progress into anaphase in the presence or absence of etoposide or veliparib. Cells were fixed and processed for IF or DNA-FISH 50 min after CDK1i washout. Unbiased imaging was performed using the field-tiling method followed by manual, non-blinded scoring of all detectable anaphases. For micronuclei analyses, MEFs were seeded in 96-well plates, treated with CDK1i as above and released into etoposide containing media. Cells were fixed 2 h post release to allow for completion of mitosis. Cells were then processed for IF and subjected to high-throughput imaging (CV7000, Yokogawa). An unbiased ImageJ detection program was used to measure the number of micronuclei and nuclei, based on size, intensity and circularity. H3K27me3 signal intensity was recorded for each micronucleus and H3K27me3 positive micronuclei were defined using a cutoff value established based on the distribution across all samples. For X-micronuclei detection using DNA-FISH, cells were grown on coverslips and treated as above. Images were blinded for unbiased, manual detection of X-micronuclei.

DNA FISH

Flow-sorted chromosome X or chromosome 2 was labeled with fluorescence tagged dUTP (Enzo Life Sciences) by DOP-PCR (degenerate oligomer-primed polymerase chain reaction) (Telenius et al., 1992). For mTFs or MEFs, cells were grown on coverslips, fixed in freshly prepared methanol:acetic acid (3:1) for 15 min, washed and stored at -20 in 70% ethanol until use. For PBMCs, cells were swollen in 75 mM KCl, fixed as above and spread on coverslips. Samples in 70% ethanol were serially dehydrated in 80, 90 and 100% ethanol, air-dried and transferred to 50% de-ionized formamide in SSC. Samples were then denatured with probes at 75°C for 2 min, incubated overnight in a humidified chamber at 37°C , washed in 0.4X SSC for 2 min at 72°C , counterstained with Hoechst 33342 and mounted using antifade. Anaphase FISH images were acquired on a Zeiss LSM780 confocal microscope. PBMC FISH images were acquired using an epi-fluorescence microscope (Imager Z2, Zeiss) and HiFish acquisition software (GenASiS, Applied Spectral Imaging, Inc., CA).

RNA-FISH and analyses

RNA FISH probes for Xist RNA FISH were prepared from full-length mouse Xist plasmid using CGH Bioprime array kit (Life Technologies, #18095011) following the manufacturer's instructions. Alexa Fluor-488 labeled dUTPs were used to label probes. Cells grown on coverslips were fixed for 15 min in 4% PFA, washed two times in PBS and stored in 70% ethanol in -20 until use. Cells were washed in PBS and in 10% formamide prior to incubating with the RNA FISH probe at 37°C overnight. Coverslips were then washed in 10% formamide and 2X SSC followed by counterstaining with Hoechst 33342 and mounting in antifade. Images were acquired using LSM 780 (Zeiss) confocal microscope and unbiased Xist detection was performed using KNIME software as described below.

Xist segmentation analyses

For Xist foci detection in male ES cells, we adapted a previously developed image analysis workflow (Jowhar et al., 2018) or detecting Xist foci in the full field of view (FOV). Briefly, the workflow uses undecimated wavelet-based spot detection algorithm (Olivo-Marin, 2002) for segmenting the Xist foci in the FOV. We used up to four wavelet scales for segmenting the Xist foci. The per-scale threshold factors were set to lower values to enable detection of all Xist signal to ensure reliable foci detection with the same set of values. Bona fide Xist foci were visually distinguished from background foci and used for quantitative assessment and comparison. Nuclear segmentation tools could not be employed in undifferentiated, colony forming cells. For Xist foci detection in differentiated female ES cells, we used the three workflows described in (Jowhar et al., 2018). Briefly, the first workflow includes a nuclear segmentation module and is followed by an interactive module which allows the end-user to annotate segmented objects into good (visually accurate segmentation) and bad (over/under segmentation) classes, calculates their morphological features, and trains a binary random forest (RF) classifier for rejecting mis-segmented nuclei (bad class). The second workflow segments nuclei in 2D, applies the trained RF classifier from previous workflow to reject mis-segmented 2D nuclei, and crops Xist foci from corresponding spectral channel(s) using the binary 2D nucleus mask. The third workflow segments Xist foci using the un-decimated wavelet-based spot detection algorithm described earlier and extracts quantitative parameters of the detected Xist foci, namely, integrated intensity (a.u.), mean intensity (a.u.), and area (pixels). The image processing steps and workflows described above were implemented into bespoke pipelines in the KNIME (Berthold et al., 2008). Analytics Platform (Version 3.2.1, 64-bit) using compatible KNIME Image Processing Nodes (Dietz and Berthold, 2016), Python and R Scripting Nodes. All KNIME workflows were either executed on a dedicated workstation running Microsoft Windows 2012 Server R2 (64-bit) with 16-cores of AMD Opteron 6212 processor (2.7 GHz) and 256 GB RAM or on a dedicated high-performance batch cluster compute node (Biowulf, CIT, NIH) running RedHat Enterprise Linux 7.4 with 28 cores of Intel X2680, 240 GB RAM, 4 K80 Nvidia GPUs and 400 GB of solid state local storage.

Spectral Karyotyping

Metaphases were arrested by incubation with Colcemid (15210-040, KaryoMax[®] Colcemid Solution, Invitrogen) ($10\ \mu\text{g/ml}$) 3 hours prior to harvest. Cells were collected and treated with hypotonic solution (KCL 0.075 M) for 15 minutes at 37°C and fixed with

methanol:acetic acid 3:1. Slides were prepared and aged overnight prior to SKY analysis. Metaphases were hybridized with the 21-color mouse SKY paint kit (FPRPR0030, ASI) according to the manufacturer's protocol. Hybridization was carried out in a humidity chamber at 37°C for 16 hours. The post-hybridization rapid wash procedure was used with 0.4X SSC at 72°C for 4 minutes. Detection was carried out following ASI manufacturer's protocol. Spectral images of the hybridized metaphases were acquired using Hyper Spectral Imaging system (Applied Spectral Imaging Inc., CA) mounted on top of an epi-fluorescence microscope (Imager Z2, Zeiss). Images were analyzed using HiSKY 7.2 acquisition software (Genesis, Applied Spectral Imaging Inc., CA). G-banding was simulated by electronic inversion of DAPI counterstaining. An average of 20 mitoses of comparable staining intensity and quality was examined per cell line and compared for chromosomal abnormality. The karyotype was determined by comparison to the standard ideogram of banding patterns for mouse chromosomes (Nesbitt and Francke, 1973). Abnormalities were then separated as either aneuploidy or other aberrations (deletions, translocations, etc.). Events were summated between autosomes and X chromosomes and the number of events for autosomes was normalized to the total number of autosomes and the number of nuclei analyzed.

Cellular extract preparation and immunoblotting

Cells were lysed in RIPA lysis buffer (150 mM NaCl, 1% NP-40, 1% Na-deoxycholate, 0.1% SDS, 25 mM Tris-HCl pH 7.5) supplemented with protease inhibitors (Sigma) and phosphatase inhibitors (Calbiochem). Lysates were sonicated, centrifuged, and heated with reducing sample buffer (375 mM Tris-HCl pH 6.8, 9% SDS, 50% glycerol, 9% β -mercaptoethanol, 0.03% bromophenol blue). Lysates of equal protein amount based on BCA assay (Thermo Fisher) were separated by SDS-PAGE and subjected to western blotting using the indicated primary antibodies. HRP-conjugated secondary antibodies were used for signal detection by enhanced chemiluminescence (Amersham).

Co-immunoprecipitation

HEK293 T-REx cells expressing Flag-tagged macroH2A1.1 or macroH2A1.2 were used for co-IP experiment along with parental cell line as control. Where indicated, PARPi was added at a concentration of 10 μ M / 6 million cells for 24 h. Equal numbers of cells were used for IP experiment. Briefly, cells were washed with PBS and resuspended in hypotonic buffer (20 mM HEPES, 10 mM KCl, 2 mM $MgCl_2$, 10% glucose, 0.5% NP-40) followed by MNase digestion (0.2 U/ μ L, 4°C, 60 min) in digestion buffer (20 mM HEPES, 150 mM KCl, 10% Glycerol, 3 mM $CaCl_2$). 20 mM EGTA was used to terminate the reaction. Using a 27G needle, each sample was aspirated 10 times followed by centrifugation at 1000 g, retrieval of the supernatant and IP with M2 magnetic beads (50% slurry) at 4°C for 60min. Post IP, beads were washed 4 times using wash buffer (20 mM HEPES, 150 mM KCl, 0.1% NP-40) followed by 50 mM HEPES. Immunoprecipitated proteins were solubilized by incubating the beads with SDS sample buffer containing 10% β -mercaptoethanol for 5 min at 95°C, followed by western blotting. LIG3 signal intensities were quantified using Image Lab software (BIO-RAD), IP intensity was normalized to input.

Digestion and dimethyl labeling of affinity purified protein complex

Affinity purified protein complexes were resuspended in 30 μ L of 25 mM HEPES (pH 8.4) and subjected to overnight digestion with 2 μ g trypsin (Promega) reconstituted in 100 mM triethylammonium bicarbonate (TEAB) (Sigma) at 37°C. Digested samples were recovered, dried and resuspended in 100 μ L of 100 mM TEAB. In-solution dimethylation of the tryptic digest was performed using CH_2O (Sigma) for light labeling or CD_2O (Sigma) for medium labeling. Labeling reagent comprising 4 μ L of 4% CH_2O/CD_2O mixed with equal amount of 0.6 M $NaBH_3CN$, was added to reconstituted tryptic digest and incubated for 1 hr at room temperature. The labeling reaction was quenched by addition of 16 μ L of 1% ammonia. Differentially labeled sample pairs were mixed, dried and de-salted using C18 spin columns (Thermo Fisher) according to the manufacturer's protocol. The peptide mixture was reconstituted in 25% ACN/0.1% FA (100 μ L) and fractionated using strong cation exchange (SCX) liquid chromatography (LC) as described in (Das et al., 2010). Thirty-six SCX fractions were pooled in 12 fractions based on the intensity profile and vacuum dried. Dried samples were reconstituted in 0.1% trifluoroacetic acid prior to MS analysis.

Mass Spectrometry acquisition and data analysis

Protein samples were subjected to nanoflow liquid chromatography (Thermo Easy nLC 1000, Thermo Scientific) coupled to high resolution tandem MS (Fusion, Thermo Scientific). MS scans were performed in the Orbitrap analyzer at a resolution of 60,000 with an ion accumulation target set at $2e^6$ over a mass range of 350-1500 m/z, followed by MS/MS analysis in an iontrap with an ion accumulation target set at $1e^5$. MS2 precursor isolation width was setup at 1.6 m/z, normalized collision energy was 29, and charge state 1 and unassigned charge states were excluded. Acquired MS/MS spectra were searched against a human uniprot protein database, using a SEQUEST and the resulting peptides were filtered at a maximum of 1% FDR using the percolator validator algorithms in the Proteome Discoverer 1.4 software (Thermo Scientific, CA). The precursor ion tolerance was set at 10 ppm and the fragment ions tolerance was set at 0.6 Da along with methionine oxidation included as a dynamic modification. For dimethyl labeling on the N terminus and lysine, 28.0313 and 32.0564 Da were filled in for light and medium labels respectively. More than 2 non-redundant peptides from each protein group was used for protein quantification.

QUANTIFICATION AND STATISTICAL ANALYSIS

Splice variant correlation analysis in NCI-60 cells

Gene expression correlation analyses across the NCI-60 panel were determined using CellMinerCDB (<https://discover.nci.nih.gov/cellminercdb/>), a web-based resource for elucidating gene expression determinants across various cancer cell line datasets (Rajapakse et al., 2018). In brief, RNA-seq transcript expression levels for a well-annotated set of repair genes were obtained from CellMiner\Query Genomic Data (<https://discover.nci.nih.gov/cellminer/queryLoad.do>). Values for macroH2A1 isoform 1.1 are based on refseq NM_138609, values for macroH2A1.2 represent the summation of NM_001040158, NM_138610, and NM_004893. The patterns for the composite gene transcript versus isoforms transcript levels were compared using Pearson's correlations, and p values were determined by two-tailed Z test using R computing (<http://www.r-project.org>).

Statistical analyses

All statistical tests and values / meaning of n are listed in the Figure legends. The following statistical tests were used as appropriate: Student's two-tailed t test, Fisher's exact test, Mann-Whitney U test, two-tailed binomial test, two-tailed Z test, ANOVA with multiple comparison assuming non-Gaussian distribution.